Computers and Structures 299 (2024) 107371

Contents lists available at ScienceDirect

Computers and Structures

journal homepage: www.elsevier.com/locate/compstruc

Efficient dynamic topology optimization of 2D metamaterials based on a complementary energy formulation

Raj Pradip Khawale [a,1], Suparno Bhattacharyya [a,1], Rahul Rai [a,b,*], Gary F. Dargush [c]

[a] *Department of Automotive Engineering, Clemson University, Greenville, SC, USA*
[b] *Department of Computer Science, Clemson University, Greenville, SC, USA*
[c] *Department of Mechanical and Aerospace Engineering, University at Buffalo (SUNY), Amherst, NY, USA*

ARTICLE INFO

Keywords:
Topology optimization
Complementary energy
Metamaterials
Computational mechanics
Structural vibration
Additive manufacturing

ABSTRACT

The advent of additive manufacturing has revolutionized the design and development of hierarchical structures, with potential applications in compliant, auxetic, and band-gap structures. This paper presents an innovative approach to developing a dynamic Topology Optimization (TO) framework for designing printable lattice structures that exhibit specific dynamic properties. Utilizing parametrically defined filament-based unit cell structures for topology optimization, we achieve desired natural frequency bandgaps in the structures composed of these unit cells. To enhance computational efficiency, we employ a complementary energy-based formulation to (semi)analytically derive the flexibility and stiffness matrices of the unit cell structure, thus, eliminating extensive finite element discretization. Consequently, a wide variety of parametrically defined filament-based meso-structures can be mathematically explored. We apply this innovative framework specifically for band-gap maximization of 2D lattice structures. By tuning the geometry within each cell using TO, we maximize the band gap. Our results show the potential of this approach to create more efficient and effective hierarchical structures with desired band-gap properties.

1. Introduction

Metamaterials are encountering growing success in various cutting-edge applications in existing and new engineering sectors [1–4]. These synthetic materials possess micro-structural patterns that exhibit unique physical behaviors or mechanical properties not found in nature [5–8]. The quest to obtain structures with desired characteristics has opened up avenues for research in diverse domains, including optics, phononics, structural engineering, and heat transfer. Metamaterials are also known as artificial lightweight structures because of their porous nature [9]. Due to the advancements in additive manufacturing, porous metamaterials of almost any geometry can be manufactured from polymers, metals, and ceramics [10,11]. Interesting applications for metamaterials involve development of compliant, auxetic or bandgap structures for use in bone regeneration and energy harvesting, to name a few [12,13]. Typically, the computational representation of metamaterials is obtained through inverse problem-solving techniques to identify the optimum structure for desired conditions.

More generally, the field of structural optimization encompasses several aspects of the inverse problem to inform the sizing, material selection, shape, and topology of structures. The initial seminal work on the topological problem is due to Michell [14], which included elegant theoretical concepts that had limited impact on practical structural design at that time. Further progress did not come until much later when computational approaches began to appear. The early work by Vanderplaats and Moses [15], Spillers and Friedland [16], and Bennett [17] focused on the topological design of truss structures. Afterwards, Bennett and Botkin [18] developed a finite element-based approach with adaptive mesh refinement for shape optimization of continuum structures. On the other hand, Bendsøe and Kikuchi [19] introduced the concept of replacing the continuum with locally-defined composite cells consisting of a solid material and voids. Then, a homogenization method was used to provide effective anisotropic elastic properties for each cell [20,21]. In this way, the original shape optimization problem was reduced to a problem of sizing and material selection. Today, most of the well-established techniques in Topology Optimization (TO) are based on this approach to solve inverse structural design

---

* Corresponding author at: Department of Automotive Engineering, Clemson University, Greenville, SC, USA.
E-mail address: rrai@clemson.edu (R. Rai).

[1] These authors contributed equally to this work.

https://doi.org/10.1016/j.compstruc.2024.107371
Received 4 December 2023; Accepted 3 April 2024

problems. Essentially, TO is an iterative method that generates an optimal structure by minimizing an objective function while adhering to constraints [22–24]. More recently, the incorporation of continuous relaxation functions and penalization techniques has reduced the reliance on homogenization, leading to the well-known Solid Isotropic Material with Penalization (SIMP) approach [25]. Different TO approaches are discussed in the monographs by Bendsøe and Sigmund [26], and Chistensen and Klarbring [27], and a popular MATLAB code was developed by Sigmund [28]. In the context of dynamic systems, TO algorithms have been employed to either decrease or increase vibrations within specific frequency ranges. For instance, clustering natural frequencies can be advantageous for energy-harvesting applications [29]. On the other hand, creating a wide gap between the natural frequencies is necessary while dealing with unsafe resonance.

With regard to TO for maximizing the frequency bandgap to mitigate vibrations within a specific frequency range, researchers have pursued two approaches: optimizing the frequency response and natural frequencies. Ma et al. [30,31] employed the homogenization method to maximize the frequency interval using both approaches. Jensen and Pedersen [32] had developed optimized 1D and 2D structures for out-of-plane waves. Tsai et al. [33] devised a technique for material distribution in structures to achieve desired mode shapes while maximizing the fundamental eigenfrequency. Lately, Lopes et al. [34] performed dynamic TO on elongated dynamic systems and validated its behavior experimentally. An optimum design of bi-material structures is generated to achieve the maximum bandgap centering at a specified frequency by Liu et al. [35]. A comprehensive review of various density-based TO methods for vibration isolation is provided in Zargham et al. [36]. However, these density-based TO methods, which result in discrete density maps as final structures, may suffer from poor manufacturability due to the limited resolution of the density map and challenges with connectivity in materials [37].

To overcome those shortcomings, researchers have also been exploring metamaterials made up of lattice structures in recent years [38–40]. Designing optimal lattice structures offers an alternative approach to density-based TO, employing repeating unit cells or lattice patterns to represent material distribution. These unit cells consist of interconnected beams or trusses arranged in a repetitive pattern [41]. In addition to their good manufacturability, lattice structures can provide more efficient load paths and effective stress distributions over density-based structures. However, the use of lattice structures for vibration isolation has been relatively limited. Syam et al. [42] identified an optimal lattice design for vibration isolation while conserving volume and verified it experimentally. Vlădulescu et al. [43] used TO to increase the fundamental frequency and reduce the total mass of a mounting bracket filled with lattices. Furthermore, Lopes et al. [44] conducted TO to achieve a frequency separation interval for bi-material lattice structures in the high-frequency domain. Beyond vibration isolators, lattice structures have significantly revolutionized the generation of optimal structures for various applications with good manufacturability.

However, the major challenges faced by the TO algorithms are due to the requirement of heavy computational processing. Since TO is an iterative method, the forward analysis, which involves identifying mechanical properties from the structure, needs to be performed in each iteration. The computational demand becomes even more intensive when dealing with lattice structures. Lattice structures require finer element discretization, making the forward analysis computationally more demanding. Researchers have predominantly relied on displacement-based Finite Element Analysis (FEA) for the forward analysis. Here, we propose a force-based method depending on the principles of Complementary Energy (CE) for parametrically-defined unit cells in lattice structures.

CE methods have a rich historical background, originating in the late 19th century with the work of Castigliano [45] on relating forces to deformations through the complementary internal energy of a structure. While displacement-based energy methods have been more widely used, various force-based complementary energy approaches have been developed over time. Monographs by Przemieniecki [46] and McGuire et al. [47] on matrix structural analysis provide comprehensive overviews of the key ideas in this field. Major early advancements in computational complementary energy methods include the seminal work by Argyris [48] on variational approaches, by Pian [49] on the introduction of stress basis functions for creating element stiffness matrices, by Patnaik [50] on the development of an integrated force method and by Felippa [51] on the formulation of complementary energy approaches using matrix algebra concepts. More recently, flexibility-based methods for beam and frame elements were utilized by Spacone et al. [52], Neuenhofer and Filippou [53] and Ladev‘eze [54]. Additionally, Boisse et al. [55], C. Zhang and Liu [56], Aref and Guo [57] and Barham et al. [58] developed the flexibility-based Large Increment Method (LIM), while Sivaselvan and Reinhorn [59] and Sivaselvan et al. [60,61] introduced and then applied the Mixed Lagrangian Formalism (MLF). The LIM and MLF approaches have several aspects in common with our present work. However, until now, the application of complementary energy and Castigliano's second theorem in TO has been limited. This approach has only been used for straight beam elements in the work of M.Liu et al. [62,63], specifically for designing a flexural hinge.

In this paper, our focus is specifically on lattice structures that consist of parametrically-defined filament structures, as depicted in Figs. 1a and 2. The use of parametric equations offers a flexible means to define the geometry of the unit cells within these structures. More importantly, the implementation of the energy-based methods for these parametric structures allows for a direct evaluation of the stiffness matrix with high accuracy, which obviates the need to perform extensive finite element discretization of the filament structures. Consequently, this CE method enables solving a relatively smaller optimization problem instead of the large-scale optimization problem resulting from finite element analysis, especially if full three-dimensional solid models are used. As will be demonstrated, the present CE approach also is more efficient than standard finite element (FE) beam element formulations.

Our earlier work [64] discussed the usage of the CE approach to estimate the effective homogenized properties of a Representative Volume Element (RVE) consisting of a parametrically defined structure. This paper presents a systematic method for stiffness matrix calculation using flexibility inversion, mass matrix formulation, and additional shear deformation for the forward analysis of lattice structures. In addition to the forward analysis, we propose the dynamic TO framework for parametrically-defined 2D lattice structures based on CE principles. We demonstrate the effectiveness of the proposed framework through the maximization of natural frequency bandgaps around a user-specified frequency. As a running example, we consider a unit cell consisting of a circular loop structure with a specific cross-section and connect the loop to the corners of a unit cell through four straight segments. The proposed TO framework is showcased on rectangular and annular macroscale domains. The important contributions of this paper can be summarized as follows:

1. Introduction of a novel structural analysis method for the topology optimization of parametrically defined lattice structures.
2. Application of the complementary energy principle to fast-compute stiffness matrices during each iteration of the optimization process leading to multifold enhancements in computational efficiency.
3. Elimination of the requirement for extensive finite element discretization.
4. Enhancement of natural frequency bandgaps in lattice structures by over 250%.

The remainder of the paper is organized in the following manner. Section 2 presents the geometry of unit cells of the lattice structure, while Section 3 discusses the derivation of the CE formulation for straight beams. TO algorithms and numerical examples considered in this paper are detailed in Section 4. Results and discussion are presented in

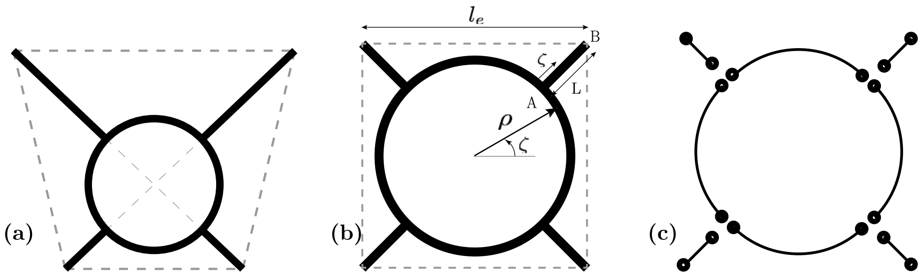

Fig. 1. Representative unit cells considered in this study. (a) Geometry of a generic quadrilateral unit cell. The gray dashed line represents the conceptual cell boundary. (b) Geometry of a unit cell with square aspect ratio. (c) Conceptual splitting of the cell into eight segments to facilitate the derivation of its stiffness matrix. Lumped masses are added to each segment for illustration only.

Sections 5, while Section 6 provides several conclusions. An appendix details the derivation of the CE formulation for curved beams.

2. Geometry of unit cells

Parametric equations offer a flexible and adaptable means to describe the geometry of the unit cells defining a lattice structure, enabling the exploration of various configurations and their effect on the overall dynamic performance of the structure. By utilizing parametrically-described unit cells, designers can manipulate the geometry during the optimization process, taking into account various dynamic constraints, such as natural frequencies, damping, and vibrational responses. This approach facilitates efficient design space exploration, considering other constraints such as weight minimization or manufacturing limitations, yet yielding efficient and robust structures that satisfy multiple performance objectives and constraints.

In this work, we consider the topology optimization of 2D structures undergoing in-plane vibration. For that we consider a quadrilateral unit cell consisting of a flexible circular loop, which is connected to four straight flexible members referred hereon as anchors. The anchors essentially lie on the diagonals of the cell and are connected to the loop where the loop intersects with the diagonals. The center of the loop always lies at the intersection of the two diagonals. A generic quadrilateral unit cell is shown in Fig. 1a.

As a more specific example, in Fig. 1b, we show a regular unit cell with square aspect ratio with length of each side as l_e, loop radius ρ, and anchor length L. Even though not necessary, it is assumed that the loop and anchors have uniform circular cross sections with a filament radius r. One cell is connected to the next using the anchors as shown in Fig. 2.

The parametric definition of the entire circular loop is given by

$$\mathbf{s}(\zeta) = \rho\cos(\zeta)\,\hat{i} + \rho\sin(\zeta)\,\hat{j} \tag{1}$$

where $\hat{i}$,$\hat{j}$, and $\hat{k}$ are the standard Cartesian unit vectors and ζ is a non-dimensional parameter, which varies between $[0, 2\pi]$. Similarly, the parametric definition of an anchor is given by

$$\mathbf{s}(\zeta) = \zeta\left(x_A - x_B\right)\hat{i} + \zeta\left(y_A - y_B\right)\hat{j} \tag{2}$$

where $\left(x_A, y_A\right)$ and $\left(x_B, y_B\right)$ are coordinates of the two ends of the anchor, and in this case, ζ varies between $[0, 1]$. We have used the same non-dimensional parametric symbol ζ to define both the circular and the straight geometry; however, they are treated independently and should not be confused.

These cells are arranged within the domain of interest, as illustrated in Fig. 2. To solve the bandgap optimization problem of the assembled structure, topology optimization is employed to modify the loop radii, resulting in the desired frequency bandgaps within the structure.

In Section 4, we describe some specific $2D$ structures composed of these cells, and the bandgap maximization of such structures. However, prior to that, in the following subsection, we discuss the response characteristics of the cell under external loading by deriving its stiffness matrix.

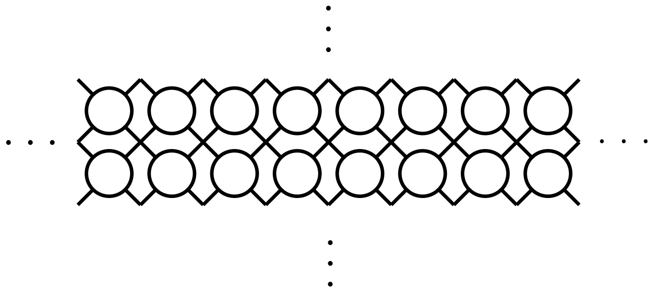

Fig. 2. Generic assembly of the unit cells.

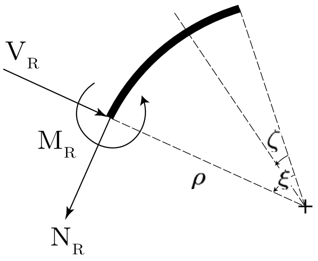

Fig. 3. Segment of a curved beam showing the shear and normal forces, and bending moment at a cross-section.

3. Cell stiffness using complementary energy

In this section, we first provide a brief overview of the complementary energy method, which serves as the foundation for the analysis framework we employ. Then, we discuss the use of complementary energy method to derive the stiffness matrix of a cell. The stiffness matrices of the cells are then assembled based on their connections within the domain, ultimately forming the stiffness matrix for the entire structure composed of cells.

3.1. Complementary energy method

The concept of complementary energy is an extension of Castigliano's 2nd theorem [45], asserting that the accurate state of stress in a structure, among all statically possible states, minimizes the total complementary energy when expressed as a function of kinetic variables. This principle is utilized here to estimate the deformation of the cell under specific loading conditions. It is determined by calculating the partial derivatives of the complementary energy of the structure relative to the applied forces and moments. Although this method applies to all elastic structures, the current study focuses on the linear elastic response under generalized Hooke's law.

Consider the schematic of a beam member shown in Fig. 3. The associated bending moment, axial force vector, and shear force at a cross section are given by $\mathbf{M_R}$, $\mathbf{N_R}$, and $\mathbf{V_R}$, respectively. Then the

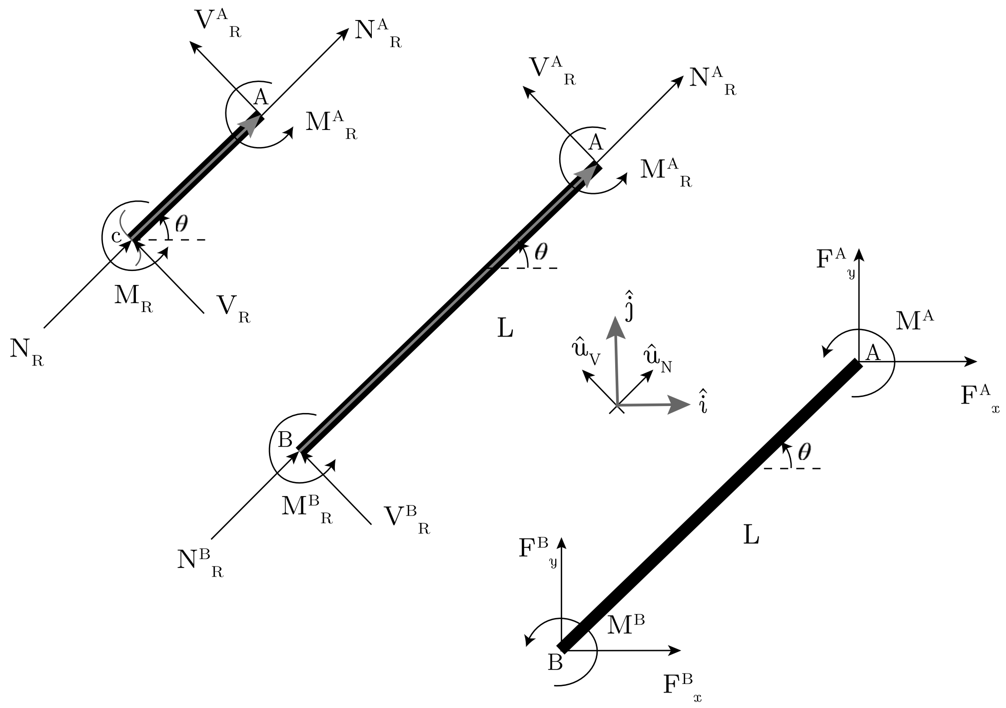

Fig. 4. Free-body diagram of a straight anchor.

internal complementary energy U^* associated with the bending, shear and axial response of the member is given by the scalar line integral

$$U^*(\xi) = \frac{1}{2}\int_0^{\xi} \left\{ \frac{\mathbf{M_R}(\mathbf{s}(\zeta)) \cdot \mathbf{M_R}(\mathbf{s}(\zeta))}{EI} + \frac{\mathbf{N_R}(\mathbf{s}(\zeta)) \cdot \mathbf{N_R}(\mathbf{s}(\zeta))}{EA_c} + \frac{\mathbf{V_R}(\mathbf{s}(\zeta)) \cdot \mathbf{V_R}(\mathbf{s}(\zeta))}{GA_s} \right\} \left|\left| \frac{d\mathbf{s}}{d\zeta} \right|\right| d\zeta \tag{3}$$

where the geometry of the member is described using some parametric definition $\mathbf{s}$, which is a function of the intrinsic variable ξ (or dummy variable ζ). Here $\cdot$ represents the inner (dot) product, E is Young's modulus of the material, G is the shear modulus, A_c is the cross-sectional area of the filament, I is the area moment of inertia of the filament cross-section, $A_s = A_c/\kappa$, where κ is the shear correction factor depending on the geometry of the cross-section, which takes into account the non-uniformity in the shear stress across the beam cross-section, and finally, $||d\mathbf{s}/d\zeta||$ is the jacobian of the transformation.

However, $\mathbf{M_R}$, $\mathbf{N_R}$, and $\mathbf{V_R}$ are essentially functions of the external forces $\mathbf{F}$ and moments $\mathbf{M}$ being applied onto the member and hence $U^*(\xi)$ can also be expressed as the following scalar function

$$U^*(\xi) = f(\mathbf{F}, \mathbf{M}) \tag{4}$$

Castigliano's second theorem based on complementary energy states that the deformation due to the external forces and moments $\mathbf{F}, \mathbf{M}$ are given by

$$\boldsymbol{\Delta}_F = \frac{\partial U^*}{\partial \mathbf{F}} \tag{5}$$

and

$$\boldsymbol{\Theta}_M = \frac{\partial U^*}{\partial \mathbf{M}} \tag{6}$$

where $\boldsymbol{\Delta}_F$ and $\boldsymbol{\Theta}_M$ represent the relative displacement and change in slope over the element due to $\mathbf{F}$ and $\mathbf{M}$, respectively. Next, we show how we can use these relations in deriving the stiffness matrix of the unit cell.

3.2. Derivation of stiffness matrix of the cell

To derive the stiffness matrix of a single cell shown in Fig. 1b with a circular loop of radius ρ, and four straight anchors of length L we adopted a *divide and conquer* approach. We divide the entire cell geometry into four quarters and four straight segments as shown in Figs. 1b and 1c. We find the stiffness matrices of each of the eight segments using the complementary energy formalism and assemble them to find the stiffness matrix of the entire assembly. Here we discuss the derivation of the stiffness matrices of one of the straight and curved segments. However, we note that the number of divisions can be suitably chosen; it need not be eight.

Let us consider the static equilibrium equation for the anchor in Fig. 4. The anchor makes an angle θ with the horizontal. In the specific case, where the unit-cell is a square (see Fig. 1b), $\theta = \pi/4$. However, we provide the analysis without ascribing any particular value to θ. As shown, the external forces and moments acting at both ends of the anchor are given by $\mathbf{F^A} = F^A_x\hat{\imath} + F^A_y\hat{\jmath}$, $\mathbf{F^B} = F^B_x\hat{\imath} + F^B_y\hat{\jmath}$, $\mathbf{M^A} = M^A\hat{k}$, and $\mathbf{M^B} = M^B\hat{k}$. The equilibrium equation for the whole anchor can be written as

$$\mathbf{p^B} = \mathsf{R}^a_{A/B}\mathbf{p^A} \tag{7}$$

where $\mathbf{p^A} = [F^A_x, F^A_y, M^A]^T$, $\mathbf{p^B} = [F^B_x, F^B_y, M^B]^T$, and $\mathsf{R}^a_{A/B}$ is given by

$$\mathsf{R}^a_{A/B} = \begin{bmatrix} -1 & 0 & 0 \\ 0 & -1 & 0 \\ r^y_{A/B} & -r^x_{A/B} & -1 \end{bmatrix} \tag{8}$$

where $r^x_{A/B}$, $r^y_{A/B}$ are the x and the y components of the position vector $\mathbf{r}_{A/B}$ from point B to A as shown in the Fig. 4 with $||\mathbf{r}_{A/B}|| = L$, the length of the anchor. We further define the external force vector $\mathbf{P} = [\mathbf{p^A}, \mathbf{p^B}]^T$ which, from Eq. (7), can be written as

$$\mathbf{P} = \mathsf{W}_a\mathbf{p^A} \tag{9}$$

where

$$\mathsf{W}_a = \begin{bmatrix} \mathrm{I}_3 \\ \mathsf{R}^a_{A/B} \end{bmatrix} \tag{10}$$

and I_3 represents the identity matrix of order 3.

In Fig. 4, the schematic in the middle shows the internal forces and moments in the anchor as result of the external forces and moments. As was described previously $\mathbf{M}^{\mathbf{A}}_{\mathbf{R}}$, $\mathbf{N}^{\mathbf{A}}_{\mathbf{R}}$, $\mathbf{V}^{\mathbf{A}}_{\mathbf{R}}$ and $\mathbf{M}^{\mathbf{B}}_{\mathbf{R}}$, $\mathbf{N}^{\mathbf{B}}_{\mathbf{R}}$, $\mathbf{V}^{\mathbf{B}}_{\mathbf{R}}$ are the bending moment, axial force vector, and shear force at cross sections A and B, respectively. To express the internal forces and moments, we adopt the coordinate systems $\hat{u}_N$, $\hat{u}_V$, and $\hat{u}_Z$. The directions of $\hat{u}_N$ and $\hat{u}_V$ correspond to the directions of the normal and shear forces, respectively. As depicted in the figure, $\hat{u}_N$ is aligned with the anchor, while $\hat{u}_V$ is perpendicular to it, whereas $\hat{u}_Z$ is perpendicular to the plane containing both $\hat{u}_N$ and $\hat{u}_V$.

The equations that relate the external and the internal forces are given by

$$\mathbf{F}^{\mathbf{A}} = \mathbf{N}^{\mathbf{A}}_{\mathbf{R}} + \mathbf{V}^{\mathbf{A}}_{\mathbf{R}} = N^A_R \hat{u}_N + V^A_R \hat{u}_V \tag{11}$$

$$\begin{Bmatrix} F^A_x \\ F^A_y \end{Bmatrix} = \begin{Bmatrix} N^A_R \cos(\theta) - V^A_R \sin(\theta) \\ N^A_R \sin(\theta) + V^A_R \cos(\theta) \end{Bmatrix} \tag{12}$$

$$\mathbf{M}^{\mathbf{A}}_{\mathbf{R}} - \mathbf{M}^{\mathbf{A}} = M^A_R \hat{u}_Z - M^A \hat{u}_Z = 0 \tag{13}$$

The above equilibrium equations can be rewritten as

$$\mathbf{p}^{\mathbf{A}} = \mathsf{S}_\theta \mathbf{q}^{\mathbf{A}} \tag{14}$$

where

$$\mathsf{S}_\theta = \begin{bmatrix} -\sin(\theta) & \cos(\theta) & 0 \\ \cos(\theta) & \sin(\theta) & 0 \\ 0 & 0 & 1 \end{bmatrix} \tag{15}$$

is an orthogonal matrix, implying $\mathsf{S}_\theta^{-1} = \mathsf{S}_\theta^T$, and $\mathbf{q}^{\mathbf{A}} = [V^A_R, N^A_R, M^A_R]^T$ represents the internal forces and moment at A. Similarly,

$$\mathbf{p}^{\mathbf{B}} = \mathsf{S}_\theta \mathbf{q}^{\mathbf{B}} \tag{16}$$

Now, the balance of the internal forces is given by

$$\mathbf{q}^{\mathbf{B}} = \mathsf{S}_\theta^T \mathsf{R}^a_{A/B} \mathsf{S}_\theta \mathbf{q}^{\mathbf{A}} \tag{17}$$

Additionally, substituting Eq. (17) in Eq. (16) we can write

$$\mathbf{p}^{\mathbf{B}} = \mathsf{R}^a_{A/B} \mathsf{S}_\theta \mathbf{q}^{\mathbf{A}} \tag{18}$$

Then, we can express the external force vector $\mathbf{P}$ using Eqs. (9), (14) and (18) as

$$\mathbf{P} = \mathsf{C}_a \mathbf{q}^{\mathbf{A}} \tag{19}$$

where

$$\mathsf{C}_a = \mathsf{W}_a \mathsf{S}_\theta \tag{20}$$

Alternatively, $\mathbf{q}^{\mathbf{A}}$ can be expressed in terms of $\mathbf{P}$ by using the Moore-Penrose pseudo-inverse C_a^+ [65]. Then,

$$\mathbf{q}^{\mathbf{A}} = \mathsf{C}_a^+ \mathbf{P} \tag{21}$$

where

$$\mathsf{C}_a^+ = \left(\mathsf{C}_a^T \mathsf{C}_a\right)^{-1} \mathsf{C}_a^T \tag{22}$$

As a result,

$$\mathsf{C}_a^+ \mathsf{C}_a = \mathrm{I}_3 \tag{23a}$$

while

$$\mathsf{C}_a \mathsf{C}_a^+ = \mathsf{W}_a \left(\mathsf{W}_a^T \mathsf{W}_a\right)^{-1} \mathsf{W}_a^T = \Lambda_a \tag{23b}$$

where Λ_a serves as a projection matrix characterized by eigenvalues 0 and 1, each with algebraic and geometric multiplicities of 3. When applied to the external force vector $\mathbf{P}$, it yields:

$$\Lambda_a \mathbf{P} = \mathsf{W}_a \left(\mathsf{W}_a^T \mathsf{W}_a\right)^{-1} \mathsf{W}_a^T \mathsf{W}_a \mathbf{p}^{\mathbf{A}} = \mathsf{W}_a \mathbf{p}^{\mathbf{A}} = \mathbf{P} \tag{24}$$

In essence, Λ_a projects $\mathbf{P}$ onto the column space $\mathrm{Col}(W_a)$, a subspace with rank 3. Given that $\mathbf{P}$ is inherently contained within $\mathrm{Col}(W_a)$, as evident from Eq. (9), the projection operation naturally retrieves $\mathbf{P}$.

Let us now consider the internal force vector $\mathbf{q} = [V_R, N_R, M_R]^T$ at an arbitrary cross-section c, ζ distance away from A, as shown in the left-most schematic of the Fig. 4. For this case, we can write the balance equations in the same way as Eq. (17)

$$\mathbf{q} = \mathsf{Q}^a \mathbf{q}^{\mathbf{A}} \tag{25}$$

where

$$\mathsf{Q}^a = \mathsf{S}_\theta^T \mathsf{R}^a_{A/c} \mathsf{S}_\theta \tag{26}$$

with

$$\mathsf{R}^a_{A/c} = \begin{bmatrix} -1 & 0 & 0 \\ 0 & -1 & 0 \\ r^y_{A/c} & -r^x_{A/c} & -1 \end{bmatrix} \tag{27}$$

and $||\mathbf{r}_{A/c}|| = \zeta$.

We now rewrite the complementary energy defined in Eq. (3) as

$$U^*(\xi) = \frac{1}{2} \int_0^\xi \mathbf{q}^T \mathsf{D} \mathbf{q} \left|\left| \frac{d\mathbf{s}}{d\zeta} \right|\right| d\zeta \tag{28}$$

where

$$\mathsf{D} = \begin{bmatrix} 1/(GA_s) & 0 & 0 \\ 0 & 1/(EA_c) & 0 \\ 0 & 0 & 1/(EI) \end{bmatrix} \tag{29}$$

Substituting Eq. (25) and the parametric equation for the straight beam Eq. (2), in Eq. (28) we get

$$U^*(1) = \frac{1}{2} \mathbf{q}^{\mathbf{A}^T} \mathcal{A}_a \mathbf{q}^{\mathbf{A}} \tag{30}$$

where we define

$$\mathcal{A}_a = \int_0^1 \mathsf{Q}^{a^T} \mathsf{D} \mathsf{Q}^a L d\zeta = \begin{bmatrix} \frac{L^3}{3EI} + \frac{L}{GA_s} & 0 & \frac{L^2}{2EI} \\ 0 & \frac{L}{EA_c} & 0 \\ \frac{L^2}{2EI} & 0 & \frac{L}{EI} \end{bmatrix} \tag{31}$$

as the flexibility matrix in terms of the internal forces at A. The integral in Eq. (31) is straightforward in this case and can be evaluated analytically; however, for a more complicated cell geometry, where the parametric equation is also complicated, these integrals may be evaluated numerically.

Now we establish the relationship between the flexibility matrix and the external forces using the complementary energy theorem, which is a crucial step in obtaining the stiffness matrix of the anchor.

Substituting Eq. (21) in Eq. (30) we get

$$U^*(1) = \frac{1}{2} \mathbf{P}^T \mathsf{C}_a^{+T} \mathcal{A}_a \mathsf{C}_a^+ \mathbf{P} \tag{32}$$

Using the complementary energy theorem Eqs. (5) and (6), and taking the partial derivative of the complementary energy with respect to $\mathbf{P}$, we obtain

$$\frac{\partial U^*}{\partial \mathbf{P}} = \mathcal{F}_a \mathbf{P} = \Delta_{\mathbf{P}} \tag{33}$$

where

$$\mathcal{F}_a = \mathsf{C}_a^{+T} \mathcal{A}_a \mathsf{C}_a^+ \tag{34}$$

is the flexibility matrix for the anchor in terms of the external forces and

$$\Delta_{\mathbf{P}} = \begin{bmatrix} \delta^A_x & \delta^A_y & \theta^A & \delta^B_x & \delta^B_y & \theta^B \end{bmatrix}^T \tag{35}$$

is the deformation vector, corresponding to $\mathbf{P}$. Finally, Eq. (33) can be rearranged using the pseudo-inverse from Eqs. (23a), (23b) and (24) to write

$$\mathcal{K}_a \Delta_{\mathbf{P}} = \mathbf{P} \tag{36}$$

where $\mathcal{K}_a \in \mathbb{R}^{6\times 6}$ is the stiffness matrix for the anchor given by

$$\mathcal{K}_a = \mathsf{C}_a \mathcal{A}_a^{-1} \mathsf{C}_a^T \tag{37}$$

So essentially the derivation of the stiffness matrix only requires the evaluations of the matrices $\mathcal{A}_a$ and C_a.

In a similar way, we can determine the stiffness matrix $\mathcal{K}_l \in \mathbb{R}^{6\times 6}$ for the quarter of the loop. However, this development is not as straightforward as it is for the anchor. We refer interested readers to the appendix for the detailed derivation.

After calculating stiffness matrices for each of the eight-segments, via an intra-matrix assembly process, we obtained a 24×24 dimensional cell stiffness matrix $\mathcal{K}_c$. Here 24 degrees of freedom correspond to three degrees of freedom at each of the four corners and four loop anchor junctions. The stiffness matrices for different cells were further assembled according to the configuration of the cells in the 2D structure to obtain the global stiffness matrix $\mathcal{K}$. For our purpose, after this intercell assembly, we reduced the stiffness matrix further by condensing the angular degree of freedom using Guyan reduction [66].

3.3. Derivation of mass matrix

During band-gap optimization, to calculate the frequency spectrum of a structure composed of unit cells, we require the mass matrix of the structure in addition to its stiffness matrix. For that, we first obtained the mass matrix of an individual cell using the lumped mass approach. In the Finite Element Method (FEM) with mass-lumping, the mass of an element is considered to be concentrated at the nodes rather than being distributed evenly throughout the element. This simplification accelerates computations, while providing accurate natural frequencies [67]. In our case, the mass of each of the segments, both curved and straight, was lumped at the two-ends of the segment, as shown in Fig. 1c. For the straight segment, namely, the anchor, the mass matrix of dimension 6×6 is given by

$$\mathcal{M}_a = \frac{1}{2}\left(\gamma \pi r^2 L_a\right) \operatorname{diag}([1,1,0]) \otimes I_2 \tag{38}$$

where, $\otimes$ denote the outer product, L_a is the length of the anchor, γ is the density of the material, and I_2 is the identity matrix of order 2. Here we ignored the effect of rotational inertial. Similarly, for the curved portion, the mass matrix is given by

$$\mathcal{M}_l = \frac{1}{2}\left(\gamma \pi r^2 L_c\right) \operatorname{diag}([1,1,0]) \otimes I_2 \tag{39}$$

where L_c is the length of the curved portion. Through an intra-assembly process, similar to what was adopted for the stiffness matrix, the mass matrices of all 8 segments were assembled to obtain the mass matrix $\mathcal{M}_c \in \mathbb{R}^{24\times 24}$ of the cell. The global mass matrix $\mathcal{M}$ was then obtained using inter-cellular assembly of $\mathcal{M}_c$. Similarly to the stiffness matrix, $\mathcal{M}$ was further reduced by condensing the angular degree of freedom using Guyan reduction.

The accuracy of the adopted complementary energy method in estimating the natural frequency of a structure is discussed in Section 5.1. In the following sections, we describe the topology optimization framework focusing on the bandgap optimization of certain structures of interest.

4. Topology optimization for bandgap maximization

In this section, we present the topology optimization (TO) framework integrated with the complementary energy formulation for designing lattice structures with specific bandgaps. We first define the optimization problem and then discuss the optimization procedure in detail.

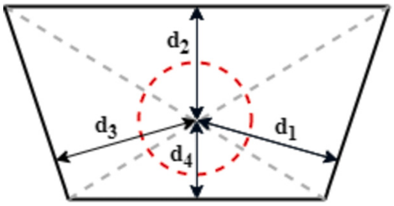

Fig. 5. Perpendicular distances between the center and each side of a quadrilateral unit cell, denoted using d_1, d_2, d_3, and d_4. The red dashed circle denotes a loop within the unit cell.

Given a design domain defined by a lattice structure consisting of parametrically defined unit cells, we aimed to tune the geometry of the individual cells to maximize the gap around a pre-specified frequency Ω_t within the natural frequency spectrum of the structure while ensuring Ω_t remains centered within this gap. The design variables in this context are the loop-radii of the unit cells. The bandgap around Ω_t is measured by taking the difference between the two natural frequencies immediately higher (ω_h) and lower (ω_l) than Ω_t. We mathematically define the optimization problem as follows:

$$\begin{aligned}
\min_{\rho_e} \quad & -(\omega_h - \omega_l) \qquad\qquad e = 1, \ldots, N_{cell} \\
\text{s.t.} \quad & \frac{1}{2}(\omega_h + \omega_l) - \Omega_t = 0 \\
& \omega_l < \Omega_t < \omega_h \\
& \rho_{min} \le \rho_e \le \rho_{max}
\end{aligned} \tag{40}$$

where ρ_e denotes the loop-radius corresponding to e^{th} unit cell, with e ranging from 1 to the total number of unit cells (N_{cell}).

The first and second constraints in Eq. (40) impose that Ω_t should lie between ω_h and ω_l and should be equal to their average, whereas the third constraint defines the upper and lower bounds of the loop-radii of the unit cells, $\rho_{\max}$ and $\rho_{\min}$, respectively. These bounds are determined based on the filament radius r and the dimension of the associated unit cells. In this study, for all cells, we selected

$$\rho_{\min} = 4r \tag{41}$$

The $\rho_{\max}$ for individual cells were computed separately, and was done by first calculating the perpendicular distances between the loop center and each of the four sides of the unit cell (shown as a generic quadrilateral in Fig. 5), denoted as d_1, d_2, d_3, and d_4, and then using the following relation, which ensured non-overlapping loops across adjacent cells:

$$\rho_{max} = \min(d_1, d_2, d_3, d_4) - r \tag{42}$$

Consequently, the total mass of the optimized structure is bounded by the mass of lattice structures with uniform loop radii of $\rho_{\min}$ and $\rho_{\max}$ across all unit cells, marking the lower and upper bounds, respectively.

We found that this constrained optimization problem can be solved efficiently, if it is posed as an unconstrained optimization problem. For this, we employed the Augmented Lagrangian Method (ALM) [68]. The ALM combines the principles of the penalty method and the Lagrangian method to solve constrained optimization problems. By incorporating penalty terms into the objective function, ALM transforms the constrained problem into a series of unconstrained subproblems. The solution of these subproblems approaches the constrained solution as the penalty parameters are increased during the solution process. For ALM, we rewrote the objective function in Eq. (40) in the following unconstrained form:

$$\min_{\rho_e} \; -(\omega_h - \omega_l) + \beta\left(\Omega_t - \frac{1}{2}(\omega_h + \omega_l)\right) + \frac{\gamma}{2}\left(\Omega_t - \frac{1}{2}(\omega_h + \omega_l)\right)^2 \tag{43}$$

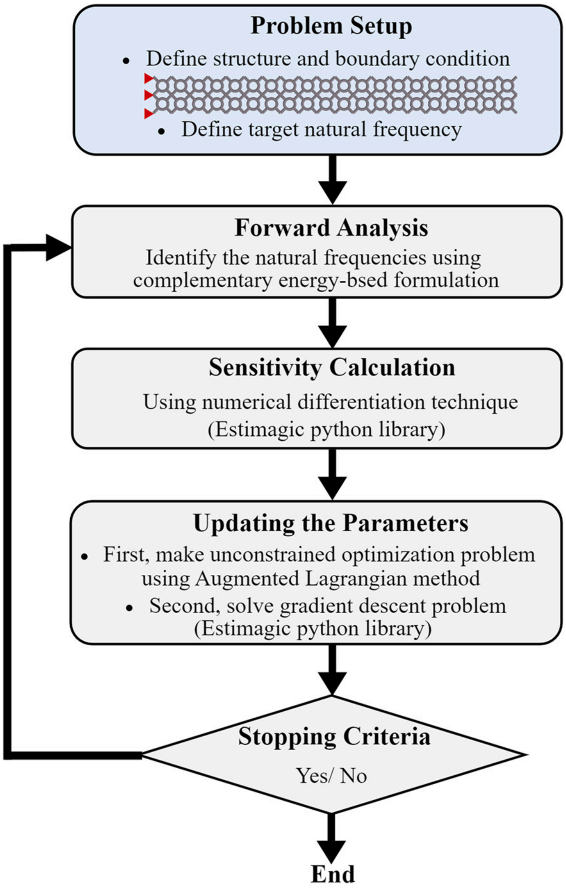

Fig. 6. Different steps in topology optimization algorithm.

where β and γ are the coefficients of Lagrangian and quadratic penalty terms. The upper and lower bounds on the radii values, however, were enforced through hard-thresholding.

The Topology Optimization (TO) algorithm was executed iteratively in three stages: forward analysis, gradient calculation, and the updating of design variables and parameters, as delineated in Fig. 6. During forward analysis, the initial radii values (within bounds) were uniformly assigned across all unit cells. Based on these radii values, the stiffness matrix and natural frequencies of the entire structure were computed, utilizing the complementary energy formulation and taking into account the pertinent boundary conditions. Subsequently, frequencies ω_h and ω_l adjacent to the target frequency Ω_t were identified and the objective function was evaluated.

With every iteration, ALM continuously updates the penalty parameters β and γ ensuring that constraints are adhered to more strictly in subsequent iterations. We used the algorithm in Johnson [68]. In each iteration, the associated unconstrained problem is solved using the Sequential Least SQuares Programming (SLSQP) optimizer. SLSQP is an iterative optimization method that operates on gradient-based principles and employs a quadratic approximation to the objective function, derived from its gradients. It then identifies a search direction that minimizes the quadratic model within the bounds defined by the constraints. The radii values were updated at every stage of iteration and this iterative refining process continued until a solution that both optimizes the objective and satisfies the constraints was found.

The SLSQP algorithm was implemented through the NLopt python library [69]. NLopt is a powerful open-source library designed for nonlinear optimization, offering a common interface for many algorithms. Moreover, in each iteration, the gradient of the objective function with respect to the radii values was calculated using the *Estimagic* python library [70].

Table 1
The geometric details of the two 2D rectangular structures considered for bandgap optimization as illustrated in Fig. 7. As described in Fig. 7. n_l and n_u denote the count of layers and the count of unit cells per layer, respectively. Additionally, L_{rect} and w indicate the length and width of the rectangular structures, respectively, while ρ_{initial} specifies the initial uniform loop radii value at the onset of the optimization process. It should be noted that the dimensions provided are unitless.

n_l	n_u	L_{rect}	w	$r(\times 10^{-3})$	ρ_{initial}
2	20	1.0	0.1	1.285	0.015
4	40	1.0	0.1	9.427	0.007

Table 2
The geometric details of the four 2D annular structures selected for bandgap optimization, as shown in Fig. 8. Here r_i and r_o denote the inner and the outer radius of the annular structure. Rest of the symbols bear the same meaning as in Table 1. Here also the dimensions are unitless.

n_l	n_u	r_i	r_o	r	ρ_{initial}
2	12	1.0	3.0	0.016	0.25
4	12	1.0	3.0	0.008	0.13
2	24	1.0	3.0	0.010	0.15
4	24	1.0	3.0	0.006	0.1

4.1. Numerical examples

We next discuss several 2D lattice structures with variations in macroscale geometries and discretization, whose bandgap optimization was performed using the proposed framework.

In this study, we investigated two types of 2D geometries: rectangular and annular. The rectangular geometry is representative of cantilever structures that are anchored at one end and free at the other, commonly found in engineering applications where considerations of load-bearing capacity and resonance are important. On the other hand, the annular geometry is characterized by a ring-like or doughnut-shaped configuration, with particular relevance to designs akin to bicycle rims. The emphasis for this latter geometry is on the strategic avoidance of specific natural frequencies to ensure structural stability of the rims in dynamic environments [71].

To investigate the influence of discretization levels on the bandgap, we examined two levels of discretization for the 2D rectangular geometry, as shown in Fig. 7, characterized by two parameters: n_l and n_u, where n_l and n_u denote the count of layers and the count of unit cells per layer in the geometry, respectively. We considered a case with (a) $n_l = 2$, $n_u = 20$, and another with (b) $n_l = 4$, $n_u = 40$. In both, the leftmost nodes are fixed, as indicated by the black triangles.

Similarly, for the annular geometry, we examined four different variations, as depicted in Fig. 8: (a) $n_l = 2$, $n_u = 12$, (b) $n_l = 2$, $n_u = 24$, (c) $n_l = 4$, $n_u = 12$, and (d) $n_l = 4$, $n_u = 24$. In the four cases, all the innermost nodes are fixed and the outer radius is three times the inner radius.

Moreover, in all of these structures, the unit cell dimensions remain uniform across each layer, even though the loop dimension within each cell can vary from one another, which is the case after optimization, as will be shown in the next section. Additional details about the geometry of these structures are provided in Tables 1 and 2. During the optimization of these structures the optimization begins with these initial configurations.

5. Results and discussion

This section is divided into two segments. Prior to discussing and presenting the optimized structures, we examine and discuss the accuracy of the CE-based framework for conducting modal analysis. Subsequently, we present the optimal structures obtained by applying the TO-framework on the structures described in Section 4.1, and their corresponding bandgaps.

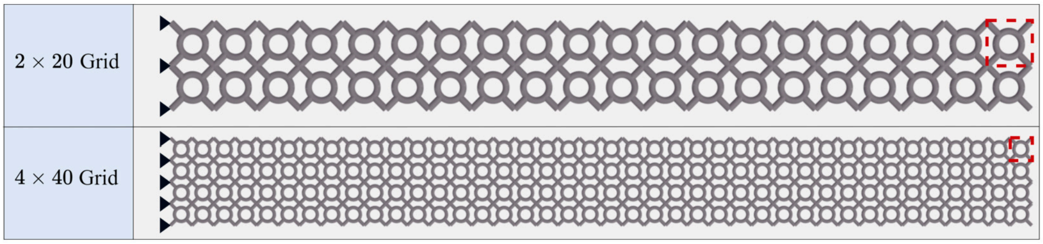

Fig. 7. The two 2D rectangular lattice structures prior to optimization. Let n_l and n_u denote the count of layers and the count of unit cells per layer, respectively. For the top structure $n_l = 2$ and $n_u = 20$ and for the structure at the bottom, $n_l = 4$ and $n_u = 40$. A representative unit cell in each structure is shown using a dashed red quadrilateral. Being cantilever structures, their left nodes are fixed, as indicated by the black triangles. Further geometric details of the structures can be found in Table 1.

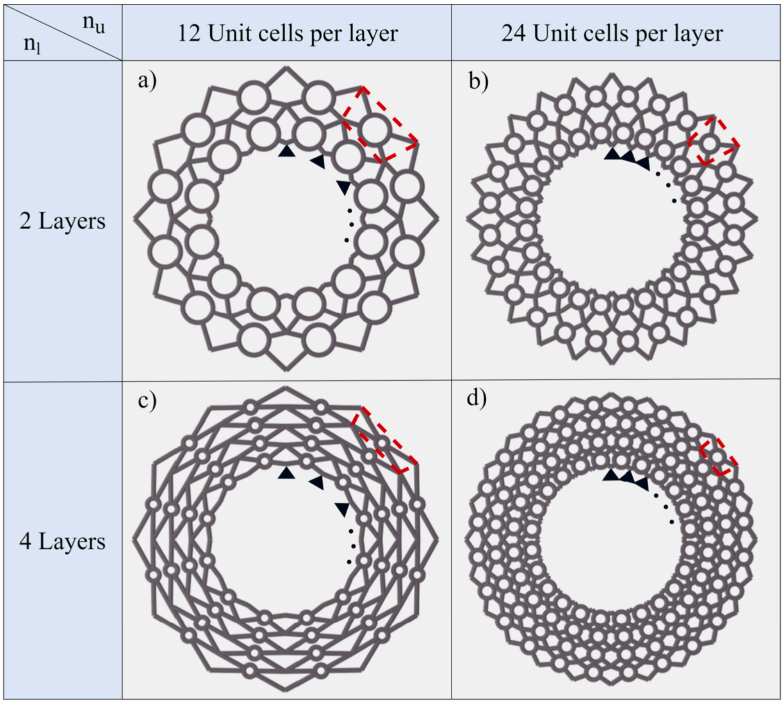

Fig. 8. The four 2D annular geometries prior to optimization with grid structures (a) $n_l = 2$ and $n_u = 12$, (b) $n_l = 2$ and $n_u = 24$, (c) $n_l = 4$ and $n_u = 12$, and (d) $n_l = 4$ and $n_u = 24$, where n_l and n_u are as defined in Fig. 7. The unit cell for each structure is denoted with a dashed red quadrilateral. A fixed boundary condition is imposed on the innermost nodes and is represented using the black triangles. Further geometric details of the structures can be found in Table 2.

5.1. Validation of CE-based framework

In the forward analysis segment of our proposed CE-based TO framework, we perform modal analysis on the structures generated by the optimization algorithm, iteratively. Hence, it is important to first assess how accurately the CE-based framework can estimate the natural frequencies of such structures. Out of the various lattice structures we experimented with, here we present the results for the 2D rectangular lattice structures akin to that shown in Fig. 7, and compare their natural frequencies obtained using the CE method with that obtained using ABAQUS [72].

Similar to Fig. 7, here we examined four levels of discretization: $n_l = 2$ and $n_u = 20$, $n_l = 4$ and $n_u = 40$, $n_l = 6$ and $n_u = 60$, and $n_l = 8$ and $n_u = 80$, while maintaining the length and width of the structures at 1 and 0.1 units, respectively. All unit cells within each level of discretization were identical, contrasting the topology optimization problem that targets inter-cellular geometry variation. The dimensions of the unit cells were determined based on the total size of the structure and the level of discretization selected. The overall volume remained constant across various levels of discretization, and the loop radius, filament radius, and anchor length within each unit cell were calculated in accordance with these geometric and discretization constraints.

For performing modal analysis in ABAQUS, each geometry was meshed with 128 B21 elements/unit cell. This number was chosen after initial experimentation and no observable difference in the results was found upon further mesh refinement. The B21 element in ABAQUS is the *Timoshenko* beam element that takes into account the transverse shear deformation, as is the case for the CE formulation in Eq. (3).

We compare the first five natural frequencies of the structures in Table 3. We see that each of the five frequencies for all four structures were estimated with high accuracy using the CE method. When compared to the results from the ABAQUS simulations, considered here as the reference, the method exhibited a minimal average difference, roughly around 0.1%. These findings confirm that the CE method can be efficiently utilized for the modal analysis of structures while significantly reducing computational cost: 8 beam segments/cell, compared to 128 beam elements/cell.

We, however, do observe that the difference in frequency estimation shows a near-decaying trend as the level of discretization increases, for all five frequency values. This suggests that differences are relatively higher at lower levels of discretization. However, it is important to clarify that this trend is not attributable to the CE method itself. Instead, it is linked to the lumped mass assumption employed in this study. The discrepancy between the lumped mass matrix of a unit cell and

Table 3

Comparison of the first five natural frequencies of different rectangular structures obtained using the complementary energy method against those obtained using ABAQUS for the four levels of discretization described in Sec. 5.1.

$n_l = 2$, $n_u = 20$			$n_l = 4$, $n_u = 40$			$n_l = 6$, $n_u = 60$			$n_l = 8$, $n_u = 80$		
Abaqus	**CE-based**		**Abaqus**	**CE-based**		**Abaqus**	**CE-based**		**Abaqus**	**CE-based**	
Freq	**Freq**	**Difference(%)**	**Freq**	**Freq**	**Difference(%)**	**Freq**	**Freq**	**Difference(%)**	**Freq**	**Freq**	**Difference(%)**
0.679	0.677	0.423	0.688	0.688	0.124	0.643	0.642	0.058	0.626	0.626	0.031
1.472	1.463	0.611	1.776	1.772	0.176	1.724	1.723	0.094	1.693	1.692	0.053
2.307	2.288	0.824	3.207	3.200	0.209	3.162	3.162	0.002	3.087	3.087	0.001
3.118	3.082	1.159	3.397	3.397	0.000	3.267	3.263	0.125	3.241	3.238	0.077
3.392	3.395	0.105	4.846	4.834	0.242	5.193	5.185	0.153	5.207	5.202	0.100

Table 4

Pre- and post-optimization bandgaps in the lattice structures.

Geometry	Configuration ($n_l \times n_u$)	Target Frequency (cycles/unit time)	Pre-optimization Bandgap	Post-optimization Bandgap	% Increase in Bandgap	% Violation of Constraint
Rectangular Geometry	2×20	76	2.392	8.521	256.23	1.034
	4×40	51	1.194	11.233	840.69	0.422
annular Geometry	2×12	1.5	0.094	0.352	274.47	0.007
	2×24	1.25	0.071	0.214	201.12	0.706
	4×12	1.2	0.093	0.284	205.38	0.000
	4×24	1.5	0.056	0.117	109.23	0.267

the actual mass matrix, as computed in ABAQUS, is more prominent at lower discretization levels. This discrepancy diminishes at higher levels of discretization as the size of the unit cells decreases. Given that natural frequency is influenced by both the mass and the stiffness matrix, this trend in difference is observed.

5.2. Bandgap analysis results

In this section, we present the results of the bandgap analysis for the structures introduced in Section 4.1. The target frequencies for both the rectangular and the annular structures shown in Figs. 7 and 8 are tabulated in Table 4. During the optimization process, the initial values for β and γ in the objective function (Eq. (43)), along with the tolerance, were set at 1, 10, and 0.1, respectively. These parameters were iteratively updated in accordance with the Augmented Lagrangian Method (ALM) algorithm outlined in Ref. [68].

In Figs. 9 and 10, we show the structures after optimization. The achieved bandgaps in their frequency spectra (within the region of interest) are shown in Figs. 11 and 12. Here the blue and red lines represent the spectra before and after carrying out the optimization, respectively. The target-frequency (Ω_t) is denoted by the dashed black line.

From Table 4, we see that post-optimization, the bandgap for the rectangular lattice structures increased more than 250%, while the constraint violation remained under 1%. The constraint violation measures the extent to which Ω_t deviates from the center of the bandgap, as stipulated by the first constraint in Eq. (40). For the annular structures, we observe an increase of more than 200% in the bandgap.

In Table 5, we present additional case studies with the 2×20 rectangular and the 2×12 annular structure, with varying target frequencies. For each structure, the post-optimization bandgaps were observed to increase notably, approximately $100 - 800\%$, with constraint violations under one percent.

The maximum achievable bandgap post-optimization largely relies on the available design space. For instance, annular structures see a smaller increase in bandgap than rectangular ones due to the comparatively limited range between the upper and lower bounds of loop radii. Furthermore, the 2×12 grid in Fig. 8a possesses fewer unit cells than the 4×24 grid structure in Fig. 8d, and hence, a fewer number of loops to optimize, but allows for more variations in tuning the loop radii. It is observed that the final bandgap for the 2×12 grid is nearly threefold compared to the 4×24 grid. This suggests that the optimization problem is influenced by the flexibility in design space more than by the quantity of variables available for optimization.

Finally, in Table 6, we demonstrate the computational efficiency of the Complementary Energy (CE) based framework relative to the traditional Finite Element (FE) method. For this comparison, we considered the 2×20 rectangular and the 2×12 annular structures depicted in Figs. 7 and 8, respectively. For the FE analysis, we used two levels of discretization: a coarse level with two elements, and a finer level with 64 elements, for each of the four curved and four straight segments in every unit cell, which resulted in total element counts of 16 and 512 per unit cell, respectively. The selection of 64 elements/segment was informed by a preliminary convergence study aimed at determining the natural frequency of the initial (pre-optimized) structures, which indicated that an increase in the number of elements beyond 64 does not significantly affect the estimates of natural frequency.

Table 6 (column 5) reveals that the topology optimization performed using the CE-based approach is nearly 25 times faster computationally than when performed using the conventional FE approach with 64 elements, for both structures. Considering that modal analysis is performed iteratively during topology optimization, this speed-up is expected since conducting a single modal analysis (done here on the initial pre-optimized structure) in the conventional approach is approximately ten times slower (refer to col. 4 of Table 6) than the CE-based analysis. Crucially, the bandgaps at the specified target frequencies were also observed to be narrower using the FE method (0.27 cycles/unit time for the 2×12 annular structure and 7.8 cycles/unit time for the 2×20 rectangular structure) compared to those achieved through the CE method (0.35 cycles/unit time and 8.5 cycles/unit time, respectively, as indicated in Table 4).

Now, to enhance the computational efficiency of the optimization process, adopting a coarser mesh can be a viable strategy, as demonstrated in Table 6, where using two elements instead of 64 resulted in an acceleration exceeding 9 times for both the annular and rectangular structures (column 4). Nevertheless, the drawback of employing a coarse mesh is its inability to accurately represent the geometry and mechanical behavior of the unit cell, leading to a compromise in precision, such as a 5.75% difference in estimating the natural frequency for the 2×12 annular structure, as highlighted in column 3. Additionally, even with this coarser discretization, the acceleration achieved with an FE-based approach falls short of the efficiency gains realized with the CE method.

The results underscore the efficiency of the CE-based framework in generating bandgaps within structures for any specified target frequency (Ω_t), in a computationally efficient manner. This approach overcomes the typical trade-off between accuracy and computational

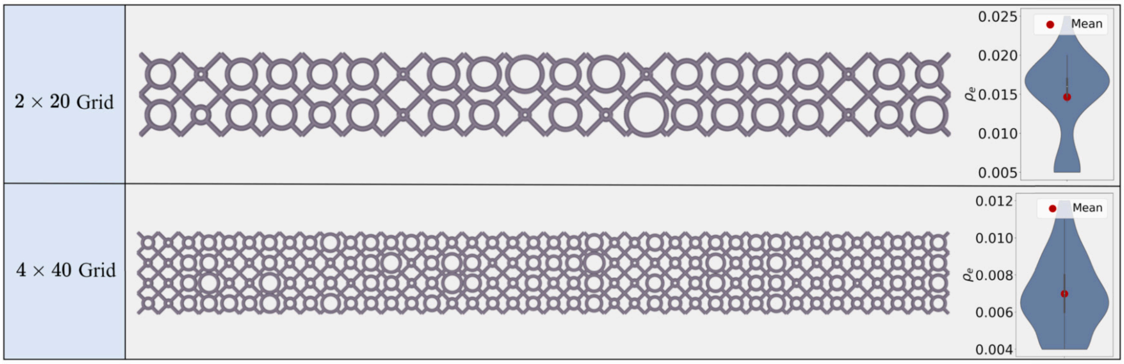

Fig. 9. Optimized rectangular structures obtained by starting from the configurations in Fig. 7 and implementing the proposed topology optimization framework. The radius values for different unit cells are diplayed using a violin plot to the right of each structure. The Red dot indicates the mean radius value.

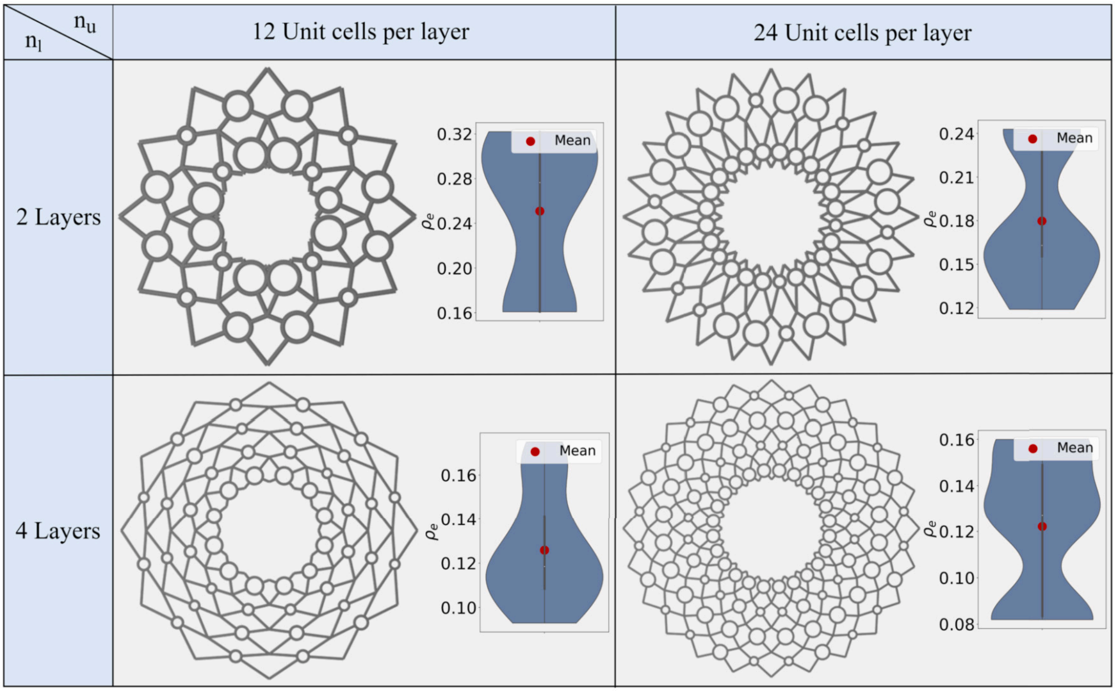

Fig. 10. Optimized annular structures obtained by starting from the configurations in Fig. 8 and implementing the proposed topology optimization framework. The radius values for different unit cells are shown using a violin plot to the right of each structure. The Red dot indicates the mean radius value.

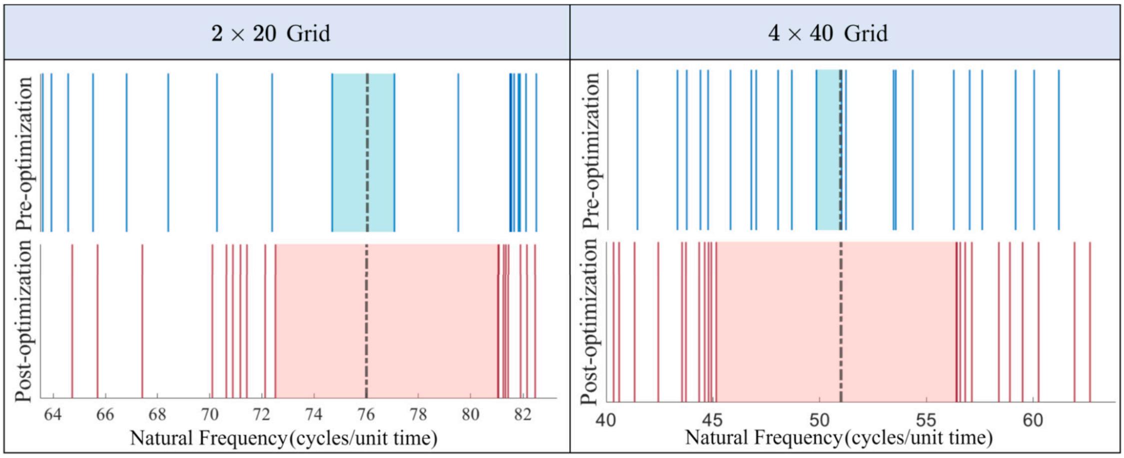

Fig. 11. Natural frequency spectra and bandgaps for rectangular structures in Fig. 9. The blue and red vertical lines denote the pre- and post-optimization natural frequencies of the structures, respectively. The black dotted lines represent the target frequency. The shaded areas indicates the bandgap around the target freqeuencies.

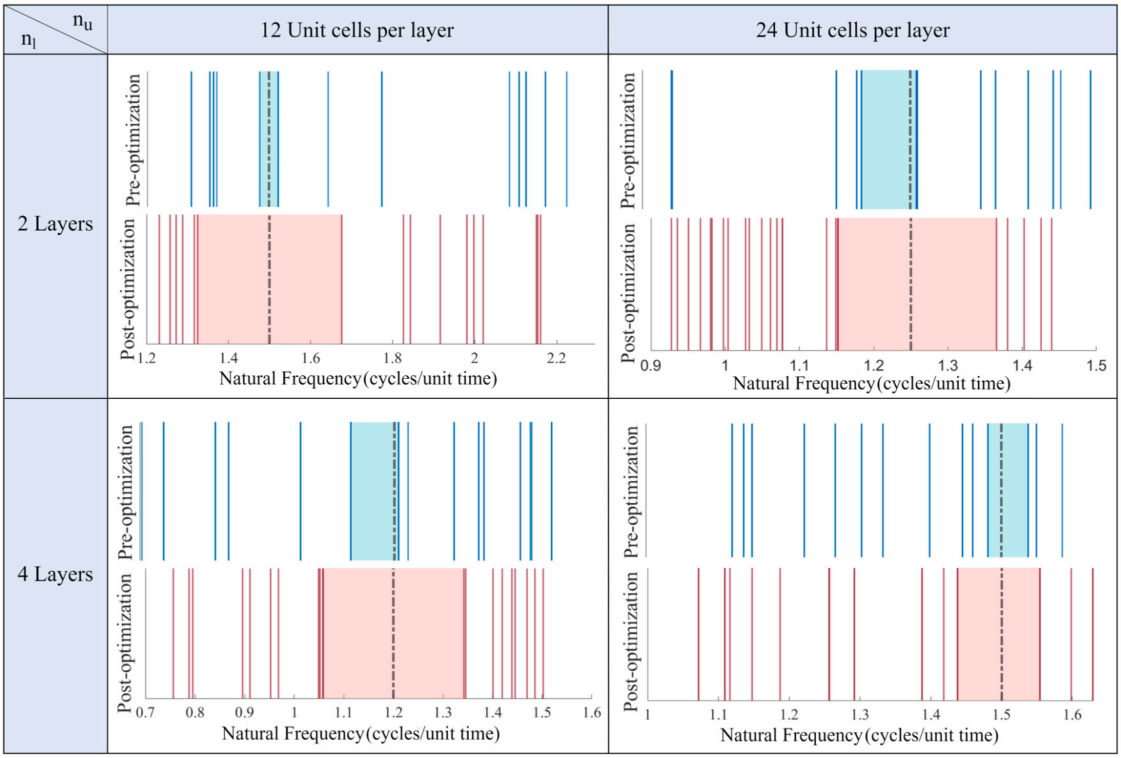

Fig. 12. Natural frequency spectra and bandgaps for annular structures in Fig. 10. The blue and red vertical lines denote the pre- and post-optimization natural frequencies of the structures, respectively. The black dotted lines represent the target frequency. The shaded areas indicates the bandgap around the target freqeuencies.

Table 5
Pre- and post-optimization bandgaps for a rectangular and an annular structure for different target frequencies.

Structure Configuration ($n_l \times n_u$)	Target Frequency (cycles/unit time)	Pre-optimization Bandgap	Post-optimization Bandgap	% Increase in Bandgap	% Violation of Constraint
Rectangular Geometry ($n_l = 2$, $n_u = 20$)	12	2.108	4.6749	121.77	0.813
	38	0.748	3.461	362.31	0.318
	110	1.825	18.616	919.72	0.097
annular Geometry ($n_l = 2$, $n_u = 12$)	2.1	0.024	0.187	676.16	0.002
	5	0.167	0.993	494.01	0.000
	0.8	0.108	0.317	193.24	0.198

Table 6
Comparison of compute times for optimization using Complementary-Energy (CE) and Finite Element (FE) based approach for a rectangular and an annular structure. Computational times for a single forward analysis are also compared. The FE computation times are shown for 16 and 512 elements per unit cell.

Structure Configuration	Forward Analysis Method		Lowest Frequency (cycles/unit time) and % Difference with CE	One Forward Analysis Time (sec)	Total Optimization Time (min)
Rectangular Geometry ($n_l = 2$, $n_u = 20$)	CE approach		0.14717	0.603	3.465
	FE approach:	512 elements	0.14716 (0.007%)	5.409	87.723
		16 elements	0.14422 (2%)	0.82	9.64
annular Geometry ($n_l = 2$, $n_u = 12$)	CE approach		0.31681	0.29	1.366
	FE approach:	512 elements	0.31683 (0.007%)	3.043	35.933
		16 elements	0.335 (5.75%)	0.47	2.025

speed encountered with the Finite Element (FE) method, offering more accurate results in less computational time.

6. Conclusion

This research focuses on the design of printable lattice structures; Specifically, we introduced a novel approach to dynamic topology optimization that can be used to efficiently design 2D lattice structures with specific dynamic properties.

For generating the lattice structures we selected filament-based unit cells. The geometry of these unit cells were tuned using a dynamic topology optimization (DTO) framework to reach a targeted natural frequency bandgap in the resulting lattice structure. This approach is demonstrated in this work using a unit cell with a circular filament loop connected to the cell corners via four straight filament segments. We employ a complementary energy (CE) based method to derive the flexibility and stiffness matrices analytically, eliminating the need for repetitive mesh-generation and excessive finite element discretization for the sake of accuracy. This not only improves computational efficiency but also opens the path to examine a broader range of filament-based meso-structures.

We implemented this method for the selective bandgap maximization of different 2D rectangular and 2D annular ring-shaped lattice structures composed of the circular loop-based unit cells. We showed that tuning the geometric parameters of the unit cells via DTO can lead to an average increase of 250% in the natural frequency bandgap, that too at a significantly higher computational speed compared to a standard FE approach.

In future work, this research can be extended in several important directions. For example, the CE methodology can be expanded to 3D lattice structures based on various other parametrically defined filament-based unit cells. As the 3D lattices have significantly more cells and beam segments, the proposed parametrically defined method can outperform more traditional methods for obtaining optimum structures by more efficiently performing simulations on thousands of structures. Furthermore, the proposed CE-based method can be easily incorporated to explore further interesting properties, such as auxeticity, negative effective mass and stiffness, and negative effective thermal coefficients of expansion. Applications to tensegrity structures and to systems exhibiting size-dependence also are possible, as are extensions to incorporate material and geometric non-linearities. CE-based approaches have already appeared for a range of these problems, as can be found in references [56–61]. Generally, we need very efficient simulation techniques, along with design tools, to obtain any of such extreme properties and advanced structural systems. This is because to explore the design space thoroughly, we may need to simulate hundreds of thousands of structures. In such situations, an efficient analysis method can accelerate property space exploration significantly. Thus, the CE framework holds much promise for deeper design space exploration and for generating structures with a wider spectrum of optimized properties.

In summary, the framework and methods presented here provide a novel approach to the design of metamaterials. Thus, this research represents an important direction for the future of hierarchical structure design, combining the strengths of additive manufacturing and topology optimization. The potential of this work to improve the efficiency and effectiveness of hierarchical structure design marks a crucial development in this rapidly evolving field.

Replication of results

The numerical models as well as the optimization framework referred herein are available from the corresponding author upon request.

CRediT authorship contribution statement

Raj Pradip Khawale: Investigation, Formal analysis, Conceptualization, Data curation, Methodology, Software, Visualization, Writing – original draft. **Suparno Bhattacharyya:** Conceptualization, Data curation, Formal analysis, Investigation, Methodology, Project administration, Software, Validation, Visualization, Writing – original draft, Writing – review & editing. **Rahul Rai:** Conceptualization, Funding acquisition, Project administration, Resources, Supervision, Writing – review & editing. **Gary F. Dargush:** Conceptualization, Formal analysis, Investigation, Methodology, Project administration, Supervision, Validation, Writing – original draft, Writing – review & editing.

Declaration of competing interest

The authors declare that they have no known competing financial interests or personal relationships that could have appeared to influence the work reported in this paper.

Data availability

Data will be made available on request.

Appendix A

In this section, we show the derivation of the flexibility matrix for a curved segment of the unit cell. Many symbols used in this section have already been defined in Section 3.2. The reader is advised to refer to Section 3.2, if needed.

Consider the curved segment shown in Fig. 13. The parametric definition of the segment is given by

$$\mathbf{s}(\zeta) = \rho\cos(\zeta)\,\hat{i} + \rho\sin(\zeta)\,\hat{j} \tag{44}$$

where the non-dimensional parameter $\zeta \in [\theta_A, \theta_B]$, θ_A and θ_B are the angles made by the two ends of the loop with the horizontal. For a square unit cell, $\theta_A = 3\pi/4$ and $\theta_B = 5\pi/4$. However, this will not be true for non-square quadrilateral unit cells. Hence, here we show how to derive a generic expression for the stiffness matrix keeping θ_A and θ_B as variables.

External forces and moments acting on both ends of the segment are given by $\mathbf{F^A} = F_x^A\hat{i} + F_y^A\hat{j}$, $\mathbf{F^B} = F_x^B\hat{i} + F_y^B\hat{j}$, $\mathbf{M^A} = M^A\hat{k}$, and $\mathbf{M^B} = M^B\hat{k}$, where $\hat{i}$,$\hat{j}$, and $\hat{k}$ are the standard Cartesian unit vectors. The equilibrium equation for the whole segment can be written as

$$\mathbf{p^B} = \mathsf{R}^l_{A/B}\mathbf{p^A} \tag{45}$$

where $\mathbf{p^A} = [F_x^A, F_y^A, M^A]^T$, $\mathbf{p^B} = [F_x^B, F_y^B, M^B]^T$, and $\mathsf{R}^l_{A/B}$ is given by

$$\mathsf{R}^l_{A/B} = \begin{bmatrix} -1 & 0 & 0 \\ 0 & -1 & 0 \\ r^y_{A/B} & -r^x_{A/B} & -1 \end{bmatrix} \tag{46}$$

with $r^x_{A/B}$, $r^y_{A/B}$ as the x and y components of the position vector $\mathbf{r}_{A/B}$ from point B to A as shown in the leftmost diagram of Fig. 13.

In Fig. 13, the schematic in the middle shows the internal forces and moments in the member as result of the external loading. As in Section 3.2, $\mathbf{M^A_R}$, $\mathbf{N^A_R}$, $\mathbf{V^A_R}$ and $\mathbf{M^B_R}$, $\mathbf{N^B_R}$, $\mathbf{V^B_R}$ are the bending moment, axial force vector, and shear force at cross sections A and B, respectively. To express the internal forces, we choose the Frenet frame, with unit vectors $\hat{u}_N(\zeta)$, $\hat{u}_V(\zeta)$, and $\hat{u}_Z$ defined as

$$\hat{u}_N(\zeta) = -\sin(\zeta)\,\hat{i} + \cos(\zeta)\,\hat{j} \tag{47a}$$

$$\hat{u}_V(\zeta) = -\cos(\zeta)\,\hat{i} - \sin(\zeta)\,\hat{j} \tag{47b}$$

$$\hat{u}_Z = \hat{u}_N \times \hat{u}_V \tag{47c}$$

The equations defining the relationships between the external and the internal forces are given by

$$\mathbf{F^i} = \mathbf{N^i_R} + \mathbf{V^i_R} = N^i_R\hat{u}_N\left(\theta_i\right) + V^i_R\hat{u}_V\left(\theta_i\right) \tag{48}$$

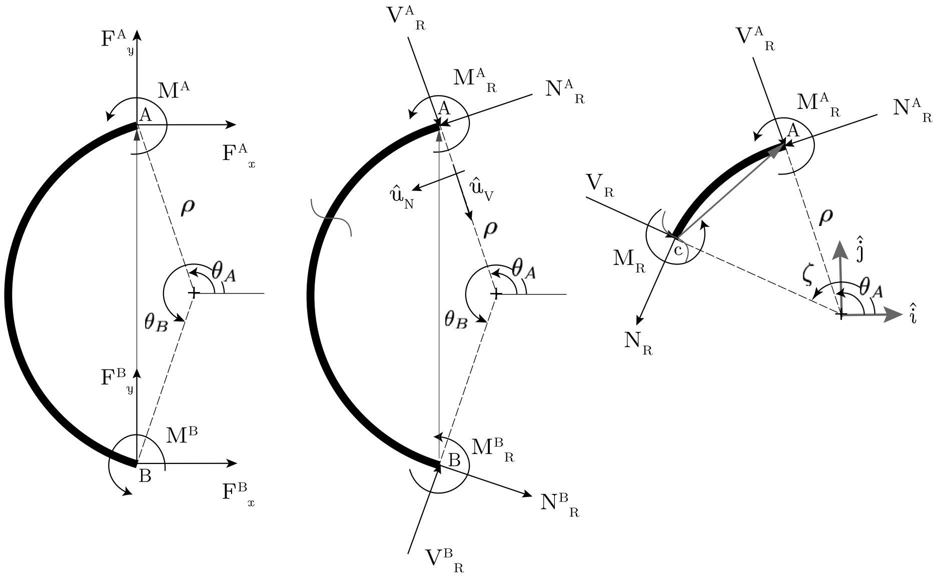

Fig. 13. Free-body diagram of a curved segment of the unit cell.

$$\mathbf{M_R^i} - \mathbf{M^i} = M_R^i \hat{u}_Z - M^i \hat{u}_Z = 0 \tag{49}$$

where $i = A, B$. The above equilibrium equations can be rewritten as

$$\mathbf{p^i} = \mathsf{S}_{\theta_i} \mathbf{q^i} \tag{50}$$

where $\mathbf{q^i} = [V_R^i, N_R^i, M_R^i]^T$ and

$$\mathsf{S}_{\theta_i} = \begin{bmatrix} -\cos(\theta_i) & -\sin(\theta_i) & 0 \\ -\sin(\theta_i) & \cos(\theta_i) & 0 \\ 0 & 0 & 1 \end{bmatrix} \tag{51}$$

Similar to Section 3.2, we define the external force vector $\mathbf{P} = [\mathbf{p^A}, \mathbf{p^B}]^T$ which, from Eq. (45), is written as

$$\mathbf{P} = \mathsf{W}_l \mathbf{p^A} \tag{52}$$

where

$$\mathsf{W}_l = \begin{bmatrix} \mathrm{I}_3 \\ \mathsf{R}^l_{A/B} \end{bmatrix} \tag{53}$$

with I_3 representing the identity matrix of order 3. From Eqs. (45) and (50), the balance of the internal forces is given by

$$\mathbf{q^B} = \mathsf{S}^T_{\theta_B} \mathsf{R}^l_{A/B} \mathsf{S}_{\theta_A} \mathbf{q^A} \tag{54}$$

Additionally, substituting Eq. (54) in Eq. (50) we can write

$$\mathbf{p^B} = \mathsf{R}^l_{A/B} \mathsf{S}_{\theta_A} \mathbf{q^A} \tag{55}$$

Then we express both the external forces $\mathbf{p^A}$ and $\mathbf{p^B}$ using $\mathbf{q^A}$ as

$$\mathbf{P} = \mathsf{C}_l \mathbf{q^A} \tag{56}$$

where

$$\mathsf{C}_l = \mathsf{W}_l \mathsf{S}_{\theta_A} \tag{57}$$

Alternatively, $\mathbf{q^A}$ can also be expressed in terms of $\mathbf{P}$ as

$$\mathbf{q^A} = \mathsf{C}_l^+ \mathbf{P} \tag{58}$$

where

$$\mathsf{C}_l^+ = \left(\mathsf{C}_l^T \mathsf{C}_l\right)^{-1} \mathsf{C}_l^T \tag{59}$$

with

$$\mathsf{C}_l^+ \mathsf{C}_l = \mathrm{I}_3 \tag{60a}$$

and,

$$\mathsf{C}_l \mathsf{C}_l^+ \mathbf{P} = \mathbf{P} \tag{60b}$$

as in Eqs. (23a), (23b), and (24). Let us now consider the internal force vector $\mathbf{q} = [V_R, N_R, M_R]^T$ at an arbitrary cross-section c. The section lies at angle ζ measured counterclockwise from the horizontal, as shown in the right-most schematic of Fig. 13. For this case, we can write the balance equations in the same way as Eq. (54)

$$\mathbf{q} = \mathsf{Q}^l \mathbf{q^A} \tag{61}$$

where

$$\mathsf{Q}^l = \mathsf{S}^T_\zeta \mathsf{R}^l_{A/c} \mathsf{S}_{\theta_A} \tag{62}$$

with

$$\mathsf{R}^l_{A/c} = \begin{bmatrix} -1 & 0 & 0 \\ 0 & -1 & 0 \\ r^y_{A/c} & -r^x_{A/c} & -1 \end{bmatrix} \tag{63}$$

and $||\mathbf{r}_{A/c}|| = 2\rho \sin((\zeta - \theta_A)/2)$.

We rewrite the complementary energy defined in Eq. (3) as

$$U^*(\xi) = \frac{1}{2} \int_{\theta_A}^{\xi} \mathbf{q}^T \mathsf{D} \mathbf{q} \left|\left| \frac{d\mathbf{s}}{d\zeta} \right|\right| d\zeta \tag{64}$$

where

$$\mathsf{D} = \begin{bmatrix} 1/(GA_s) & 0 & 0 \\ 0 & 1/(EA_c) & 0 \\ 0 & 0 & 1/(EI) \end{bmatrix} \tag{65}$$

Substituting the parametric equation for the curved beam as in given in Eq. (44) and Eq. (61) in Eq. (64) we get

$$U^*(\theta_B) = \frac{1}{2} \mathbf{q^A}^T \mathcal{A}_l \mathbf{q^A} \tag{66}$$

where we define

$$\mathcal{A}_l = \int_{\theta_A}^{\theta_B} \mathsf{Q}^{l^T} \mathsf{D} \mathsf{Q}^l \left|\left| \frac{d\mathbf{s}}{d\zeta} \right|\right| d\zeta \tag{67}$$

as the flexibility matrix for the curved segment in terms of internal forces at A. Using Eqs. (60a), (60b) and (66), and following Section 3.2, the stiffness matrix $\mathcal{K}_l$ is obtained as

$$\mathcal{K}_l = \mathrm{C}_l \mathcal{A}_l^{-1} \mathrm{C}_l^T \tag{68}$$

We were able to find a large analytical expression for the stiffness matrix $\mathcal{K}_l$ using *Mathematica* [73], which we chose to omit here. However, an expression for the flexibility matrix $\mathcal{A}_l$ is given below. In many cases, it may not be possible to obtain a closed form solution of Eq. (67). In that case, one can still evaluate the integral numerically. Since $\mathcal{A}_l$ is symmetric, we may write it as a lower triangular matrix, as follows:

$$\mathcal{A}_l = \begin{bmatrix} \mathcal{A}_l(1,1) & \text{sym} & \text{sym} \\ \mathcal{A}_l(2,1) & \mathcal{A}_l(2,2) & \text{sym} \\ \mathcal{A}_l(3,1) & \mathcal{A}_l(3,2) & \mathcal{A}_l(3,3) \end{bmatrix}$$

where:

$$\mathcal{A}_l(1,1) = \frac{1}{8}\left(\frac{-\sin(2\Delta\theta)+2\Delta\theta}{EA} + \frac{4\Delta\theta T_1^2}{EI} + \frac{\sin(2\Delta\theta)+2\Delta\theta}{GA_s}\right)$$

$$\mathcal{A}_l(2,1) = \frac{1}{4}\left(\frac{\sin^2(\Delta\theta)}{EA} + \frac{2\Delta\theta T_1 T_2}{EI} - \frac{\sin^2(\Delta\theta)}{GA_s}\right)$$

$$\mathcal{A}_l(2,2) = \frac{1}{8}\left(\frac{\sin(2\Delta\theta)+2\Delta\theta}{EA} + \frac{4\Delta\theta T_2^2}{EI} + \frac{-\sin(2\Delta\theta)+2\Delta\theta}{GA_s}\right)$$

$$\mathcal{A}_l(3,1) = -\frac{\Delta\theta T_1}{2EI}$$

$$\mathcal{A}_l(3,2) = -\frac{\Delta\theta T_2}{2EI}$$

$$\mathcal{A}_l(3,3) = \frac{\Delta\theta}{2EI}$$

The terms used in the matrix are defined as:

$$\Delta\theta = \theta_2 - \theta_1$$

$$S_1 = \sin(\theta_1)$$

$$C_1 = \cos(\theta_1)$$

$$\Delta x = x_A - x_B$$

$$\Delta y = y_B - y_A$$

$$T_1 = S_1\Delta x + C_1\Delta y$$

$$T_2 = -C_1\Delta x + S_1\Delta y$$

References

[1] Colabella L, Cisilino AP, Fachinotti V, Kowalczyk P. An efficient strategy to implement local porosity constraints in the multiscale design of solids with parameterized biomimetic microstructures. Comput Struct 2023;285:107084.

[2] Khawale RP, Bhattacharyya S, Bielecki D, Rai R, Dargush G. Efficient methods for flexibility-based meso-scale dynamic modeling. In: Society for experimental mechanics annual conference and exposition. Springer; 2023. p. 125–7.

[3] Plocher J, Panesar A. Review on design and structural optimisation in additive manufacturing: towards next-generation lightweight structures. Mater Des 2019;183:108164.

[4] Coulais C, Overvelde JT, Lubbers LA, Bertoldi K, van Hecke M. Discontinuous buckling of wide beams and metabeams. Phys Rev Lett 2015;115(4):044301.

[5] Cui Y, Takahashi T, Matsumoto T. An exact volume constraint method for topology optimization via reaction–diffusion equation. Comput Struct 2023;280:106986.

[6] Li P, Yang F, Liu Y, Bian Y, Zhang S, Wang L, et al. Design of dual-phase lattice materials with balanced modulus, strength and energy absorption properties based on sudoku arranged reinforcement phase distribution. Comput Struct 2023;286:107093.

[7] Bertoldi K, Vitelli V, Christensen J, Van Hecke M. Flexible mechanical metamaterials. Nat Rev Mater 2017;2(11):1–11.

[8] Hanks B, Berthel J, Frecker M, Simpson TW. Mechanical properties of additively manufactured metal lattice structures: data review and design interface. Addit Manuf 2020;35:101301.

[9] Berger J, Wadley H, McMeeking R. Mechanical metamaterials at the theoretical limit of isotropic elastic stiffness. Nature 2017;543(7646):533–7.

[10] Askari M, Hutchins DA, Thomas PJ, Astolfi L, Watson RL, Abdi M, et al. Additive manufacturing of metamaterials: a review. Addit Manuf 2020;36:101562.

[11] Rafsanjani A, Pasini D. Bistable auxetic mechanical metamaterials inspired by ancient geometric motifs. Extreme Mech. Lett. 2016;9:291–6.

[12] do Rosário JJ, Berger JB, Lilleodden ET, McMeeking RM, Schneider GA. The stiffness and strength of metamaterials based on the inverse opal architecture. Extreme Mech. Lett. 2017;12:86–96.

[13] Liao G, Luan C, Wang Z, Liu J, Yao X, Fu J. Acoustic metamaterials: a review of theories, structures, fabrication approaches, and applications. Adv Mater Technol 2021;6(5):2000787.

[14] Michell AGM. The limits of economy of material in frame-structures. Philos Mag 1904;8:589–97.

[15] Vanderplaats GN, Moses F. Automated design of trusses for optimum geometry. J Struct Div 1972;98(3):671–90.

[16] Spillers WR, Friedland L. On adaptive structural design. J Struct Div 1972;98:2155–63.

[17] Bennett JA. Topological structural synthesis. Comput Struct 1980;12(3):273–80.

[18] Bennett J, Botkin M. Structural shape optimization with geometric description and adaptive mesh refinement. AIAA J 1985;23(3):458–64.

[19] Bendsøe MP, Kikuchi N. Generating optimal topologies in structural design using a homogenization method. Comput Methods Appl Mech Eng 1988;71(2):197–224.

[20] Nishiwaki S, Frecker MI, Min S, Kikuchi N. Topology optimization of compliant mechanisms using the homogenization method. Int J Numer Methods Eng 1998;42(3):535–59.

[21] Arabnejad S, Pasini D. Mechanical properties of lattice materials via asymptotic homogenization and comparison with alternative homogenization methods. Int J Mech Sci 2013;77:249–62.

[22] Ben-Yelun I, Saucedo-Mora L, Sanz MÁ, Benítez JM, Montans FJ. Topology optimization approach for functionally graded metamaterial components based on homogenization of mechanical variables. Comput Struct 2023;289:107151.

[23] Liu M, Wang Y, Wei Q, Ma X, Zhang K, Li X, et al. Topology optimization for reducing stress shielding in cancellous bone scaffold. Comput Struct 2023;288:107132.

[24] Wang J, Panesar A. Machine learning based lattice generation method derived from topology optimisation. Addit Manuf 2022;60:103238.

[25] Rozvany GI, Zhou M, Birker T. Generalized shape optimization without homogenization. Struct Optim 1992;4:250–2.

[26] Bendsøe MP, Sigmund O. Topology optimization. Springer Berlin Heidelberg; 2004.

[27] Christensen PW, Klarbring A. An introduction to structural optimization. Dordrecht, Netherlands: Springer; 2009.

[28] Sigmund O. A 99 line topology optimization code written in matlab. Struct Multidiscip Optim Apr. 2001;21:120–7.

[29] Wein F, Kaltenbacher M, Stingl M. Topology optimization of a cantilevered piezoelectric energy harvester using stress norm constraints. Struct Multidiscip Optim 2013;48:173–85.

[30] Ma Z-D, Kikuchi N, Hagiwara I. Structural topology and shape optimization for a frequency response problem. Comput Mech 1993;13(3):157–74.

[31] Ma Z-D, Cheng H-C, Kikuchi N. Structural design for obtaining desired eigenfrequencies by using the topology and shape optimization method. Comput Syst Eng 1994;5(1):77–89.

[32] Jensen JS, Pedersen NL. On maximal eigenfrequency separation in two-material structures: the 1d and 2d scalar cases. J Sound Vib 2006;289(4–5):967–86.

[33] Tsai T, Cheng C. Structural design for desired eigenfrequencies and mode shapes using topology optimization. Struct Multidiscip Optim 2013;47:673–86.

[34] Lopes HN, Cunha DC, Pavanello R, Mahfoud J. Numerical and experimental investigation on topology optimization of an elongated dynamic system. Mech Syst Signal Process 2022;165:108356.

[35] Liu P, Zhang X, Luo Y. Topological design of freely vibrating bi-material structures to achieve the maximum band gap centering at a specified frequency. J Appl Mech 2021;88(8).

[36] Zargham S, Ward TA, Ramli R, Badruddin IA. Topology optimization: a review for structural designs under vibration problems. Struct Multidiscip Optim 2016;53:1157–77.

[37] Wang J, Chen WW, Da D, Fuge M, Rai R. Ih-gan: a conditional generative model for implicit surface-based inverse design of cellular structures. Comput Methods Appl Mech Eng 2022;396:115060.

[38] Li M, Song Y, Yang X, Zhang K. Lattice structure design optimization under localized linear buckling constraints. Comput Struct 2023;286:107112.

[39] He J, Kushwaha S, Abueidda D, Jasiuk I. Exploring the structure-property relations of thin-walled, 2d extruded lattices using neural networks. Comput Struct 2023;277:106940.

[40] Yang J, Su H, Li X, Wang Y. Fail-safe topology optimization for multiscale structures. Comput Struct 2023;284:107069.

[41] Molnár G, Blal N. Topology optimization of periodic beam lattices using cosserat elasticity. Comput Struct 2023;281:107037.

[42] Syam WP, Jianwei W, Zhao B, Maskery I, Elmadih W, Leach R. Design and analysis of strut-based lattice structures for vibration isolation. Precis Eng 2018;52:494–506.

[43] Vlădulescu F, Constantinescu DM. Lattice structure optimization and homogenization through finite element analyses. Proce Inst Mech Eng Part L, J Mater Des Appl 2020;234(12):1490–502.

[44] Lopes HN, Mahfoud J, Pavanello R. High natural frequency gap topology optimization of bi-material elastic structures and band gap analysis. Struct Multidiscip Optim 2021;63:2325–40.

[45] Castigliano A. Théorie de l'équilibre des systèmes élastiques et ses applications, vol. 1. AF Negro; 1879.

[46] Przemieniecki JS. Theory of matrix structural analysis. Courier Corporation; 1985.

[47] McGuire W, Gallagher RH, Ziemian RD. Matrix structural analysis. second edition. CreateSpace Independent Publishing Platform; Jan. 2015.

[48] Argyris J. Energy theorems and structural analysis. part i: General theory. Aircr Eng 1954;26:347–56. 383–387.

[49] Pian TH. Derivation of element stiffness matrices by assumed stress distributions. AIAA J 1964;2(7):1333–6.

[50] Patnaik S. An integrated force method for discrete analysis. Int J Numer Methods Eng 1973;6(2):237–51.

[51] Felippa CA. Will the force method come back? J Appl Mech 1987.

[52] Spacone E, Ciampi V, Filippou F. Mixed formulation of nonlinear beam finite element. Comput Struct 1996;58(1):71–83.

[53] Neuenhofer A, Filippou FC. Geometrically nonlinear flexibility-based frame finite element. J Struct Eng 1998;124(6):704–11.

[54] Ladevèze P. Nonlinear computational structural mechanics: new approaches and non-incremental methods of calculation. Springer Science & Business Media; 2012.

[55] Boisse P, Ladevèze P, Rougée P. A large time increment method for elastoplastic problems. Eur J Mech A, Solids 1989;8(4):257–75.

[56] Zhang C, Liu X. A large increment method for material nonlinearity problems. Adv Struct Eng 1997;1(2):99–110.

[57] Aref AJ, Guo Z. Framework for finite-element–based large increment method for nonlinear structural problems. J Eng Mech 2001;127(7):739–46.

[58] Barham W, Aref AJ, Dargush GF. Development of the large increment method for elastic perfectly plastic analysis of plane frame structures under monotonic loading. Int J Solids Struct 2005;42(26):6586–609.

[59] Sivaselvan MV, Reinhorn AM. Lagrangian approach to structural collapse simulation. J Eng Mech 2006;132(8):795–805.

[60] Sivaselvan MV, Lavan O, Dargush GF, Kurino H, Hyodo Y, Fukuda R, et al. Numerical collapse simulation of large-scale structural systems using an optimization-based algorithm. Earthq Eng Struct Dyn 2009;38(5):655–77.

[61] Oliveto N, Sivaselvan M. Dynamic analysis of tensegrity structures using a complementarity framework. Comput Struct 2011;89:2471–83.

[62] Liu M, Zhang X, Fatikow S. Design and analysis of a high-accuracy flexure hinge. Rev Sci Instrum 2016;87(5):055106.

[63] Liu M, Zhang X, Fatikow S. Design of flexure hinges based on stress-constrained topology optimization. Proc Inst Mech Eng, Part C, J Mech Eng Sci 2017;231(24):4635–45.

[64] Bielecki D, Rai R, Menasco WW, Dargush GF. Complementary energy based meso-level homogenization for multiscale topology optimization. Struct Multidiscip Optim 2023;66:156.

[65] Ben-Israel A, Greville TNE. Generalized inverses: theory and applications. 2nd edition. New York: Springer; June 2003.

[66] Guyan RJ. Reduction of stiffness and mass matrices. AIAA J Feb. 1965;3(2):380.

[67] Bathe K-J. Finite element procedures. second edition. Watertown, MA: Klaus-Jürgen Bathe; Aug. 2014.

[68] Bierlaire M. Optimization: principles and algorithms. 2nd ed. Lausanne: EPFL Press; 2018.

[69] Johnson SG. The nlopt nonlinear-optimization package; 2014.

[70] Gabler J. A python tool for the estimation of large scale scientific models; 2022.

[71] Sasaki Y, Takahashi K, Tomiyama K, Hagiwara T, Watanabe K. Development of a bicycle vibration model for road surface roughness evaluation. J Jpn Soc Civil Eng, Ser E1 (Pav Eng) 2018;74(3).

[72] Dassault Systemés Simulia Corp.. Abaqus unified FEA; 2022. Version 2022.

[73] Wolfram Research Inc. Mathematica, Version 12.0. Champaign, IL. 2023.